**Contract No.:**

This manuscript has been authored by Battelle Savannah River Alliance (BSRA), LLC under Contract No. 89303321CEM000080 with the U.S. Department of Energy (DOE) Office of Environmental Management (EM).

# Effects of Selenium Doping in Zinc Telluride from First Principles

Jonathon N. Baker*, Utpal N. Roy

Savannah River National Laboratory, Aiken, SC 29808, USA

**Abstract**

Point defects and compensation in zinc telluride have been subjects of study for several decades due to the compound's scientific/technological applications. Despite this, there remains some disagreement in the literature as to the fine details of its defect chemistry. Recently, it has also come under renewed interest due to the emerging $Cd_{(1-x)}Zn_xTe_{(1-y)}Se_y$ material family, used in nuclear radiation detector applications. In this article, we use state-of-the-art computational tools to re-examine the native defect chemistry of ZnTe and explore how it changes upon addition of selenium, using density functional theory with screened hybrid exchange-correlation functionals, thermochemical models of the equilibration environment, and statistical mechanics models of the point defects ensemble.

**Keywords:** density functional theory, materials modeling, defects, dopants, doped semiconductors, II-VI semiconductors

* Corresponding author email: jonathon.baker@srnl.doe.gov

**Introduction**

Zinc telluride is a II-VI chalcogenide semiconductor with a direct bandgap of about 2.2 eV at room temperature. It adopts the zincblende crystal structure, with interpenetrating FCC lattices of anions and cations. On its own, it is typically used in opto-electronics, nonlinear optics, and, recently, has been proposed as a cryogenic scintillator for radiation detector applications.[1-4] It is also one of the endmembers of and precursor compounds used in the production of CdZnTe and CdZnTeSe radiation detectors, which are able to operate at room temperature.[5, 6] CdZnTe has long been known as the most promising commercial material for room temperature radiation detector applications. However, the material contains severe performance limiting defects that hinders realization of large volume detectors at reasonable cost. Recently it was observed that partially replacing Te with selenium in CdZnTe matrix successfully mitigates many of these defects.[7, 8]

The native point defect behavior of ZnTe has been the subject of numerous investigations over the past 60 years, all with differing methodologies, but with almost universal agreement that the zinc vacancy plays a dominant role, and somewhat less universal agreement about what other types of point defects are present, with reports of tellurium vacancies , cation interstitials, and antisites all coming from various authors[9-14]. For radiation detector and solar cell applications, however, the identity, characteristics, and concentrations of these other defects are critical, as information on the zinc vacancy alone is insufficient to fully understand the range of trapping centers that will be present. Additionally, many authors have reported extreme difficulty in production of n-type ZnTe.[2, 9-11, 13, 15-19] This is a trend that has continued from the very first investigations of the material up to the present, and is so much an issue that when ZnTe *is* made n-type, that is often a significant result itself.[2, 17, 19] Finally, with recent interest in multicomponent II-VI alloys, many containing selenium, such as $Cd_{(1-x)}Zn_xTe_{(1-y)}Se_y$, $Cd_{(1-x)}[V|Fe|Mn]_xTe$, $Cd_{(1-x)}Zn_xTe_{(1-y)}Mn_y$, and $Mn_{(1-x)}Zn_xTe_{(1-y)}Se_y$, it has become especially important to understand how alloy constituents behave throughout the composition space; data on this, especially in the dilute limit, is severely lacking.[6, 20-28]

In order to improve the understanding of defect chemistry in ZnTe, which is an end member to many of the chalcogenide systems coming under renewed interest and therefore a pre-requisite for improving understanding of the defect chemistry in the alloyed host matrices, and to understand how selenium might impact ZnTe at sub-alloying concentrations, we have applied advanced computational methods to study the ZnTe material system and its behavior when doped with selenium. It is expected that, in addition to providing a more refined model of the defect chemistry in ZnTe and Se:ZnTe, these results may be generalized to some extent in order to better understand potentially unanticipated effects when introducing same-group substitutionals expected to be electrically neutral.

To this end, we apply methods combining Density Functional Theory (DFT), thermochemical modeling, and statistical mechanics for simulating the native and Se-containing point defects in ZnTe and their concentrations under various processing conditions and upon their quench to room temperature, as well as the resultant concentrations of the free charge carriers. Density functional theory is used to obtain ground state and vibrational contributions to defect formation energies, thermochemical models are used to obtain the chemical potentials of native species corresponding to experimentally relevant melt-growth, and statistical mechanics is used to obtain the point defect and charge carrier populations at equilibration temperature and upon quenching to room temperature. In order to improve the accuracy of the data being used in the statistical mechanics simulations above standard DFT-informed

point defect methods, the employed thermochemical models take into account the complete temperature change of the chemical potential space, rather than using the ground state space, and vibrational contributions have been taken into account for high and medium concentration defects (>$10^{13}$ $cm^{-3}$). Although these are typically considered to be second-order contributions to the defect behavior, they can have subtle but important effects on the balance between point defects and complexes and on the overall compensation behavior of the material system.

From the results, in addition to the refined defect chemistry models we present, three main conclusions are drawn: (1) it is not only difficult to make n-type ZnTe, it is actually *impossible*, at least from a high temperature near-equilibrium melt (2) in addition to incorporating as an alloying constituent on the Te sublattice, a minority of added Se incorporates as a charged substitutional and a charged complex with the native vacancies; (3) there is a threshold amount of selenium, well below the dilute limit, above which these minority forms of Se will begin affecting the charge balance and trapping behavior.

**Theoretical Methods**

All Density functional theory (DFT) calculations were performed with VASP 6 using a 2x2x2 **k**-point mesh.[29-31] Ground state calculations for the bandstructure, a high resolution density of states, bulk and thermodynamic reference phases, and all point defects listed in table 1 were performed with a plane wave kinetic cutoff of 520 eV and the Heyd-Scuseria-Ernzerhof 2006 (HSE06)[32, 33] screened hybrid exchange-correlation functional with an exact exchange amount of 0.318. This value was chosen to correct for the underestimation of the bandgap common to traditional functionals, using the work of Isik *et al* as a reference.[34] The density of states was calculated with 100,000 energy bins and an 11x11x11 **k**-point mesh. Force constant matrix calculations for select defects were performed with a plane wave kinetic energy cutoff of 700 eV and the Perdew-Burke-Ernzerhof (PBE) exchange-correlation functional. Projector Augmented Wave pseudopotentials were used with 12, 6, and 6 electrons explicitly simulated for Zn, Te, and Selenium, respectively. 72 and 108 atom tetrahedral supercells were used for isolated point defects and point defect complexes, respectively, and atoms within 5 Å of each defect center were allowed to relax.

Vibrational energy changes for some point defects were obtained from force constant matrix calculations within the harmonic approximation, as the difference in vibrational free energies between bulk and defective supercells of the same size and using an 11x11x11 **q**-point mesh. These defects are marked with a * in table 1 and were selected because their calculated concentrations (see below for description of method) were higher than $10^{13}$ $cm^{-3}$ when calculated with only HSE06 (Heyd-Scuseria-Ernzerhof-2006 screened hybrid exchange-correlation functional) data. These direct differences in vibrational energy capture how the phonon ensemble of a given point defect differs from that of the bulk---in other words, it isolates the defect-specific portions of the vibrational spectrum. These direct differences are not balanced against exchange of atoms and electrons with the relevant thermodynamic reservoirs, and should only be used to calculate differences in formation energy as part of equation 5, below. A brief description of calculating vibrational energies within the harmonic approximation and of transforming the force constant matrix to the dynamical matrices and integrating across momentum space may be found in the work of Togo.[35] The Minimal Phonon Library (MPL), a module of the Asphalt Point Defect Informatics System, was used for the harmonic approximation calculations, **q**-point integration of thermodynamic properties, and integration of the vibrational properties with the point defect thermodynamics.[36]

*Table 1: Simulated Defects and Defect Charge States*

| Defect | Charge States | Defect | Charge States |
|---|---|---|---|
| $v_{Zn}$* | -3…1 | $Zn_{Te}$ | -2…2 |
| $v_{Te}$* | -1…3 | $Te_{Zn}$* | -2…2 |
| $v_{Zn}$-$v_{Te}$* | -2…1 | $Te_{Zn}$-dx | -2…2 |
| $Zn_{int\text{-}4Te}$ | 0…3 | $Se_{Te}$* | -1…1 |
| $Zn_{int\text{-}4Zn}$ | 1…3 | $Se_{Zn}$ | 1…4 |
| $Te_{int\text{-}4Te}$ | -2…0 | $Se_{Zn}$-dx | -2…2 |
| $Te_{int\text{-}4Zn}$ | -2…2 | $Se_{vZn\text{-}vTe}$* | -1…1 |

The chemical potentials and their changes with temperature are calculated based on the method described in Baker *et al* [37], whereby the ground state energies of the host (ZnTe) and reference (Zn and Te) phases are used to construct a simplex of the chemical potentials (shown for ZnTe in equation 1, below) which is then perturbed by temperature- and pressure-dependent changes to the host and reference chemical potentials at the equilibration conditions (equations 2 and 3 below). Experimental thermochemical data is taken from Barin and the NIST-JANAF thermochemical tables.[38, 39] When needed, low temperature data is calculated from DFT simulations using MPL in the harmonic approximation, as described above.

$$\mu_{ZnTe} = \mu_{Zn} + \mu_{Te}, \text{ where } \mu_i = \mu_i^o + \Delta\mu_i \text{ and } \mu_i^o = \frac{1}{n_i} \cdot E_{tot}^i \quad \textbf{(1)}$$

$$\Delta H_{f,0K}^{ZnTe} + G^{ZnTe}|_{0K}^{T} = \Delta\mu_{Zn} + \Delta\mu_{Te} \quad \textbf{(2)}$$

$$G^i\Big|_{0K}^{T,P} \geq \Delta\mu_i \quad \textbf{(3)}$$

For this work, the relevant equilibration conditions are those corresponding to Traveling Heater Method (THM) growth parameters, which is typically conducted for chalcogenide tellurides in the vicinity of 800-850°C. The ingots are grown from a Te-rich melt, where the Te-rich melt zone is sandwiched between the seed/grown crystal and a polycrystalline feed ingot (ZnTe for the case of ZnTe growth). The molten zone is translated upwards either by lowering the ampoule or moving the heater upwards. During the process, the upper part of the zone, which is at higher temperature, dissolves the material from the polycrystalline ingot and deposits the excess material at the seed/grown ingot (near the growth interface) near the lower part of the zone which is at lower temperature. Since the crystals are grown from a Te-rich melt, the THM ingots can be grown well below the melting point of the grown material. The THM process is further detailed elsewhere.[40] ZnTe phase diagrams place the ZnTe-Te liquidus at 10-15 at% Zn in the range of 800-850°C (10 at% Zn at 800°C).[41, 42] Therefore, a dissolved zinc content of 10 atomic percent and a growth temperature of 800°C was assumed throughout the manuscript, unless noted otherwise.

Thus, $\Delta\mu_{Te}$ and $\Delta\mu_{Zn}$are calculated for the case of molten tellurium in equilibrium with solid ZnTe and containing (unless noted otherwise) 10 atomic percent dissolved Zn, using the method described above to account for finite temperature changes to internal energies and phase, and including ideal solution effects with Raoult's law (shown below in equation 4, where $\Delta\mu_i^*$ gives the ideal solution contributions to the chemical potentials and $x_i$ is the mole fraction of component i).

$$\Delta\mu_i^* = k_B T ln(x_i) \quad \textbf{(4)}$$

The bandgap contraction with temperature is calculated with the single phonon model using Isik's parameters for the effective phonon mode's energy and Huang-Rhys factor, while the individual band edge movements are calculated according to the derivation from the Bose-Einstein formulae reported by Harris.[34, 43] When calculated as a unitless fraction of the total bandgap contraction, Harris's derivation yields temperature-independent fractions, in this case of 0.204 for the VB and 0.796 for the CB. The formation energy of a defect in a given charge state is given by equation 5, below:

$$E_{D^q}^f = \left(E_{D^q}^{tot} + E_{D^q}^{corr}\right) - E_{bulk}^{tot} + \Delta E_{D^q}^T - \sum_i n_i\mu_i + q\left(E_f + E_{VB}\right) \quad \textbf{(5)}$$

In this equation, $E_{D^q}^{tot}$ is the total DFT energy of the defective cell, $E_{bulk}^{tot}$ is the total DFT energy of the bulk cell, and $E_{D^q}^{corr}$ is a finite size correction accounting for potential alignment and any electrostatic cross-boundary interactions, in this case based on the work of Kumagai and Oba and using the experimental low temperature relative dielectric constant 10.4.[44, 45] Equation 6, below, gives the general form of this correction, where $E_{PC}$ is the point charge correction and $q\Delta V_{PC,q/b|far}$ is an alignmentlike term which corrects for the potential difference between the defective and bulk cells, sans contributions from point charge effects. Returning to equation 5, the term $\sum_i n_i\mu_i$ accounts for atoms exchanged between the defect cell and the respective grand canonical reservoir to create the defect. The term $q\left(E_f + E_{VB}\right)$ describes the energy change involved in exchanging electrons between the defect and the rest of the material, given by the Fermi level $E_f$ plus the energy of the valence band maximum $E_{VB}$, scaled by the number of electrons being exchanged $q$. Lastly, $\Delta E_{D^q}^T$ is the change in defect energy with temperature from all effects except configurational entropy; the configurational entropy is instead accounted for in the prefactors of the Maxwell-Boltzmann exponentials. As magnetic and electronic entropies are tertiary contributions to dilute point defect energies at best, $\Delta E_{D^q}^T$ is set to $(\Omega_{D^q} - \Omega_{bulk})$, the difference in the grand potentials of the phonon ensembles in the defective and bulk cells within the harmonic approximation, which is itself generally expected to only be a second order contribution.[46]

$$E_{D^q}^{corr} = E_{PC} - q\Delta V_{PC,q/b|far} \quad \textbf{(6)}$$

$$[D^q] = N_s N_c e^{-E_{D^q}^f/(k_B T)} \quad \textbf{(7)}$$

$$[n] = \int_{E_{CB}}^{E_{CB}^{top}} g(\mathcal{E})F(\mathcal{E},T)d\mathcal{E} \quad \textbf{(8)}$$

$$[p] = \int_{E_{VB}^{bottom}}^{E_{VB}} g(\mathcal{E})[1 - F(\mathcal{E},T)]d\mathcal{E} \quad \textbf{(9)}$$

$$[p] - [n] + q_{D^q}\sum_{D^q}[D^q] = 0 \quad \textbf{(10)}$$

All of this data is then used to calculate the point defect concentrations using Maxwell-Boltzmann statistics as has been described previously.[36, 47] This is done by self-consistently calculating the Fermi level, defect populations, and charge carrier populations under full equilibrium which satisfy the charge neutrality condition and impurity doping levels, with chemical potentials corresponding to THM growth and taking bandgap contraction and the full set of defect formation energies into account. This solution is then further used to self-consistently solve for the Fermi level and the defect and charge carrier populations after the system is cooled to room temperature, by allowing the defect populations to change their ionization states to maintain charge neutrality. The equations for point defect

concentrations, charge carrier concentrations, and the condition of charge neutrality are given above for the reader's convenience, as equations 7-10, where $N_s$ and $N_C$ are the number of available sites and the number of geometrically degenerate geometries of the defect in the lattice, g(Ɛ) is the number of available states at energy level Ɛ, and F(Ɛ, T) is the Fermi Dirac function.

**Results & Discussion**

Figure 1a and 1b show the formation energies of the simulated defects at low (25°C, (a)) and high (800°C, (b)) temperatures versus the Fermi level. The native chemical potentials for these subfigures are calculated for molten Te containing 10 at% dissolved Zn in equilibrium with solid ZnTe at 800°C. The x-axis in these subfigures shows the Fermi level relative to the valence band maximum at the corresponding temperature. Changes to the point defect energies, in gap levels, and carrier band extrema with temperature may therefore be read off from these subfigures. Selenium containing defects are shown for a selenium concentration of $10^{19}$ $cm^{-3}$ (.0288 at%). This concentration was chosen because it is a power of 10 close to, but still below, the changeover between native-defect-controlled and selenium-modified defect chemistry regimes. The Fermi levels computed with the statistical mechanics simulations for these conditions are about 0.61 eV for Figure 1(b), under full equilibrium at 800°C, and about 0.16 eV for figure 1(a), under re-ionization of the solution for 1(b) at room temperature. It should also be noted that, as ZnTe and ZnSe form a continuous solid solution, no Se-containing precipitates or competing phases need be considered here.[48]

Figure 1c shows how the in-gap state levels (the points where the formation energy lines change slope, also referred to as the thermodynamic transition levels and charge transition levels) change with temperature for those defects having had their vibrational contributions simulated (indicated with stars in Table 1). In-gap states in 1a and 1b correspond to discrete points on the lines in Figure 1c at room temperature and 800°C. The y-axis shows the in-gap state energy and carrier band extrema relative to the ground state valence band maximum, with temperature as the x-axis.

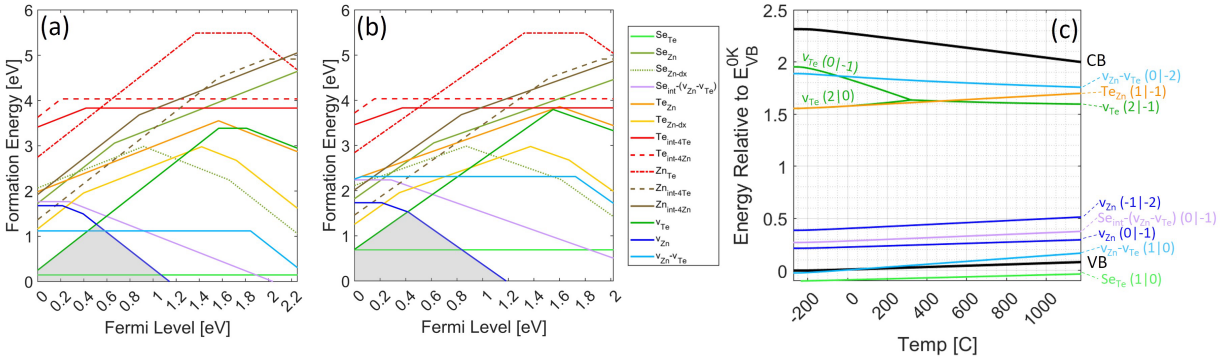


*Figure 1 (a,b) Formation Energies of simulated point defects at room temperature (a) and 800°C (b), including band edge movement and vibrational energy contributions [for starred defects in table 1]; Zn and Te chemical potentials are calculated for molten Te containing 10 at% dissolved Zn at 800°C in equilibrium with solid ZnTe, while selenium defects are shown for a concentration of Se=$10^{19}$ $cm^{-3}$. (c) In-gap state levels of simulated point defects, and their changes with temperature [for starred defects in table 1].*

The formation energies of native defects move up and down with respect to each other as the chemical potentials of the processing environment change, per the term $\sum_i n_i \mu_i$ in eq. 5, while the formation energies of selenium containing defects will move down (lower formation energy) with higher selenium concentration and up (higher formation energy) with lower selenium concentration. For the Traveling Heater Method (THM)-relevant growth conditions shown in Figure 1, the native zinc and tellurium vacancies ($v_{Zn}$ (blue) and $v_{Te}$ (dark green)) are seen to dominate, with transitions at 0.23 and 0.41 eV, and 1.5 and 1.82 eV above the valence band at room temperature, respectively. The divacancy complex is not, to the author's knowledge, a defect which has been previously speculated on in the literature, despite the prevalence of impurity-vacancy complexes in chalcogenides. It consists of a first nearest neighbor bound pair of anion and cation vacancies, and has a formation energy between that of the native vacancies it is composed of and higher energy defects such as antisites and interstitials. While it is neutral for much of the bandgap, it displays a deep (0|-2) transition near the conduction band, and a shallow (1|0) transition that emerges at high temperature near the valence band. The $v_{Zn}$ levels maintain a relatively constant separation from each other with increasing temperature, as shown in Fig. 1c, and a relatively constant distance to the valence band, meaning that the depth of their level with respect to the valence band edge does not change very much. The $v_{Te}$ levels, on the other hand, actually combine into a single level once the temperature increases above about 300°C (dark green line in Fig. 1c), and neither the individual nor the combined levels track with either band edge. The zinc vacancy's formation energy changes very little with temperature, and both native vacancies shift much less with temperature than the divacancy complex $v_{Zn}$-$v_{Te}$, whose dramatic increase in formation energy with temperature [from vibrational effects] greatly limits its concentration. These differences in behavior arise from differences in the strain fields around the ground state defects, which manifests as differences in the phonon spectrum properties. Specifically, $v_{Zn}$ only creates a very slight distortion field, and its degree is fairly uniform across changing charge states. Meanwhile, $v_{Te}$ exhibits a much larger lattice distortion, strongly bowing out surrounding atoms in its +2 charge state and strongly bowing them in in its -1 charge state, although the distortion field in the neutral and +1 charge states are much smaller and more in line with that created by the zinc vacancy. The divacancy complex distortion field is effectively a more strain-relieved, combined version of the strain fields of the $v_{Zn}$ and $v_{Te}$ defects, with a greatly increased vibrational free energy contribution. This greater temperature dependence for the divacancy may be physically rationalized as being caused by synergistic effects of the strain fields along with the larger vacancy volume as compared with the isolated vacancies.

In these conditions, the $Se_{Te}^{0}$ defect is low in formation energy, as it should be at such a high selenium concentration. This being the most dominant form of selenium reflects the fact that selenium can be readily alloyed with ZnTe to form a random solid solution on the tellurium sublattice. The selenium-divacancy complex (Fig 1a-c, purple line), which consists of a selenium atom sitting within a divacancy void, exhibits a single in-gap state which rests at 0.28 eV above the valence band at room temperature and which, like the zinc vacancy, moves at roughly the same speed as the valence band. It should be noted that, geometrically, this defect consists of a zinc vacancy complexed with a selenium substitutional; however, for conceptual clarity, as this is the end-state of simulations beginning from both ($v_{Te}$-$Se_{Zn}$) and ($v_{Zn}$-$Se_{Te}$), it is instead referred to as $Se_{int}$-($v_{Zn}$-$v_{Te}$). Lastly, there are a number of antisite and interstitial defects having overall higher formation energies than any of these, at least for the processing conditions studied; these are shown in Figure 1 for completeness. The implications of this regarding speculation in the literature as to which defects typically accompany the zinc vacancy are discussed below.

The low formation energies of $v_{Zn}$ and $v_{Te}$ actually fundamentally limit the material to be p-type only at high temperature equilibrium processing conditions and, through the more complicated set of relationships governing re-ionization, after cooling to room temperature. We find this to be true even for the most Zn-rich conditions accessible within our equilibrium space, and even in the presence of idealized donor dopants. In a formation energy diagram, under full equilibrium conditions, the Fermi level is constrained to lie inside the polyhedra formed by native defects; such regions for THM grown ZnTe are indicated with shading in figures 1a and 1b. Physically, the movement of the Fermi level past such a boundary would result in the concentration of whichever native defect it moved past rapidly increasing and destabilizing the material. While there is no such physical constraint on the behavior after cooling, the low temperature defect chemistry typically reflects that of the high temperature in at least the majority carrier type, since the same ionization states are still available but without the ability to change the overall defect concentrations. While these diagrams correspond to ZnTe crystallizing from a tellurium-enriched melt, similar regions in the formation energy diagram, and the same p-type constraint, exist for ZnTe in equilibrium with zinc vapor.

In conditions on the more Zn-rich side of the chemical potential space, the shaded area under the vacancy shifts to the right. However, the magnitude of this shift is only large enough to shift this shaded region to the middle of the formation energy diagram. Even under the influence of an idealized donor dopant at $10^{21}$ $cm^{-3}$, the zinc vacancy forces the Fermi level back down to, at best, insulating behavior at room temperature, for any set of conditions within the equilibrium chemical potential spaces corresponding to growth from a high temperature melt. This is the reason that n-type ZnTe has remained elusive while p-type ZnTe is trivial: because it is not actually possible to make n-type ZnTe with high temperature, near-equilibrium techniques, due to the unique interplay between the chemical potential space movements with temperature and the behavior of the native vacancies.[2, 17-19]

The same data as used when generating the formation energy diagrams and the in-gap level versus temperature diagram have been used to explicitly calculate point defect and carrier concentrations, shown in figure 2. The rows correspond to temperatures (high/low), while the columns correspond to processing parameters (equilibration temperature, dissolved zinc content, selenium content). More specifically: Figures 2a and 2b show the charge carrier and defect concentration versus freeze-in temperature figures 2c and 2d show the same versus zinc content in the melt, and figures 2e and 2f show the charge carrier and defect concentrations versus selenium content. Figures 2c-2f are computed for an equilibration temperature of 800°C. While many production techniques make use of slow cooling instead of a fast quench, in general, once the system reaches a temperature below which the defects can no longer diffuse quickly, it may be considered to fast quench below that point. This temperature, whether arising from defect mobility freeze-out or fast-quenching, is referred to here as the freeze-in temperature.

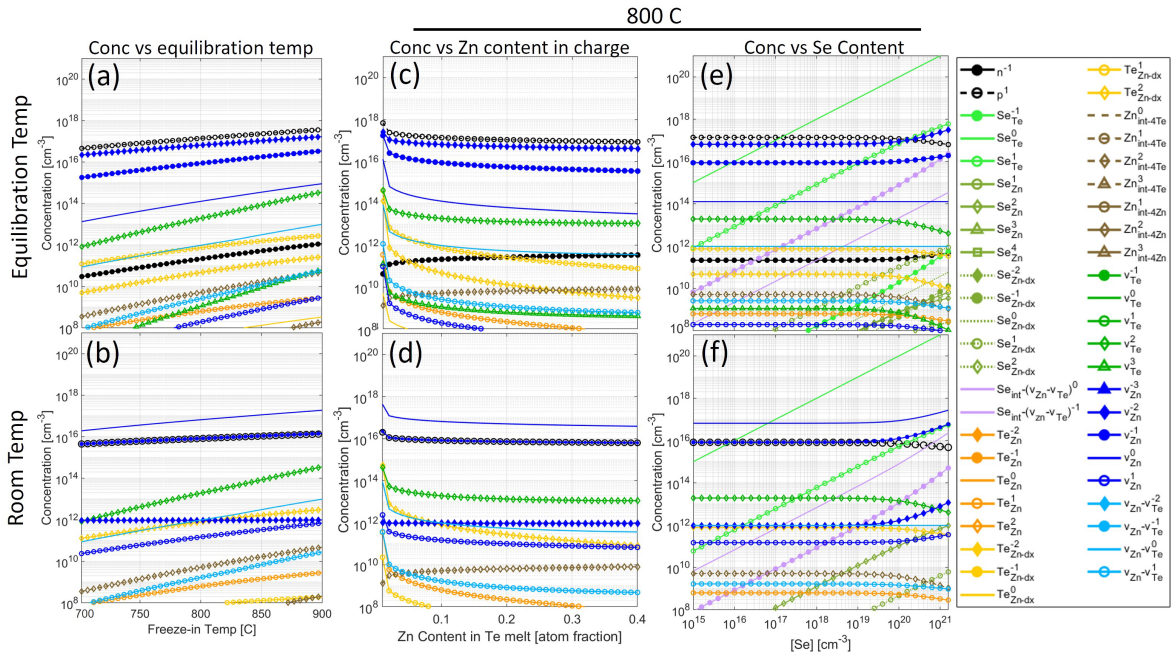


*Figure 2: High (top: a, c, e) and low (bottom: b, d, f) temperature defect (colored lines) and charge carrier (black lines) concentrations predicted for ZnTe quenched from (a,b) a 10 at.% Zn tellurium melt at increasing freeze-in temperature, (c,d) a tellurium melt with increasing amounts of dissolved zinc content, (e,f) a 10 at.% Zn tellurium melt with increasing selenium content, up to about 3 at%. Defects are color coded by type, with the marker indicating the charge state (see legend to right).*

The calculated room temperature hole concentrations and its trends versus equilibration temperature (Fig2b), are in excellent agreement with literature measurements for similarly processed, high-purity material, being in the high $10^{15}$-low $10^{16}$ $cm^{-3}$ range for Te-rich conditions, and increasing with increasing equilibration temperature.[9, 15] The underlying physics and chemistry driving this are however complex. Increasing temperature leads to **(a)** increasingly negative Zn and Te chemical potentials and **(b)** a general increase in overall point defect concentrations due to a smaller thermodynamic β $\left({}^{1}/_{k_B T}\right)$, which are partially counterbalanced by **(c)** a $v_{Te}$ population which increases faster, proportionally, than $v_{Zn}$ as the Fermi level is pulled lower at higher temperatures due to the charge balance, albeit at too low of a magnitude to outweigh increases in $v_{Zn}$ concentration from effects (a) and (b). The room temperature hole concentration thus steadily increases with freeze-in temperature, along with the major point defects (Fig 2a,b). However, the room temperature hole concentration steadily decreases with increasing zinc concentration in the melt (Fig2c,d), finally dropping to around an order of magnitude less at 90 at.% zinc (not shown) than at 0 at.% Zn. This trend is seen experimentally in the work of Smith, albeit with samples containing an unknown impurity at $10^{17}$ $cm^{-3}$, and for anneals under Zn-rich vapor rather than changes in charge composition.[13] The primary native defect in all cases is acceptor-like $v_{Zn}$, as expected from the literature, albeit with an electrically neutral form making up most of the population. $v_{Te}$ is found to act as a donor and is found to contribute to the charge balance as the second highest population native defect, with it and the free holes counter-balancing the charged $v_{Zn}$ population. The large population of neutral $v_{Zn}$ may seem counter-intuitive when estimating the compensation behavior solely from the lowest defect crossings in the formation energy diagrams (figures 1a and 1b), as is often done. However, the re-ionization constraint needed to calculate concentrations at room temperature can lead to very different results for the system's charge neutrality condition from what might be

assumed with such an estimate. A full self-consistent statistical mechanics model able to take re-ionization into account, as employed in this work, is necessary to accurately calculate defect concentrations in such cases. It is noteworthy, however, that testing with an idealized donor dopant shows that for cases where the doping or impurity profiles are, on balance, donor-like, the dominant zinc vacancy charge state shifts to -2.

Lower concentration defects include the Te antisite and various interstitials, as have been speculated by some prior authors to be primary or secondary defects, as well as the divacancy complex. The third and fourth most populous defects in this system are seen to be the divacancy complex and the $Te_{Zn\text{-}dx}$ anti-site, although their order depends somewhat sensitively on the processing conditions. Higher solute levels in the melt and higher temperature can both shift this balance more in favor of the divacancy. The highest concentration interstitial, $Zn_{int\text{-}4Te}$, is never more than the fifth most common defect. So, in one sense, the disagreement in the literature about which native point defects are present in ZnTe has some merit, in that they are all present at some level, at least in these simulation results. However, in these simulations, $v_{Te}$ is always the second most populous native point defect. This remains true even for simulations (not shown) corresponding to equilibration with Zn-rich vapor.

Figures 2e and 2f deal with the defect chemistry under increasing amounts of selenium. While by far the majority of the selenium incorporates as neutral $Se_{Te}$, as intuitively expected based on the existence of $ZnTe_xSe_{(1-x)}$ alloy, charged selenium defects incorporate at a level beginning at $1/1000^{th}$-$1/10000^{th}$ of the overall Se content, with the exact fraction depending on the freeze-in temperature. These charged defects take two forms. The higher concentration minority Se defect is $Se_{Te}^{1}$, a selenium substitutional on a tellurium site which has captured a hole. This transition level does not exist in the gap proper, instead being buried slightly below the valence band. Despite this, it is present in appreciable quantities due to the Fermi level being pulled low due to the simple Arrhenius behavior of concentration versus Fermi level. This isolated level likely only exists because, while selenium and tellurium have the same number and configuration of valence electrons, selenium is only populated up to the $4^{th}$ shell, whereas tellurium is populated up to the $5^{th}$. The smaller energy of the 4p states dictates that, until the selenium reaches a high enough concentration to fully hybridize with the tellurium frontier orbitals (i.e. beyond the dilute limit), its highest occupied state will exist at an energy slightly below tellurium's. In cases where the doping or impurity profile is overall donor-like in character, this state will not be present, as the Fermi level will be too far from the valence band to activate it. There is an even lower concentration form of selenium present as well: the selenium-divacancy complex. These complexes are present at levels several thousand to several hundred thousand times lower than the overall Se level, with the exact value again depending on the freeze-in temperature, and exhibit both a deep trap state and a moderate geometric distortion. Because of the vicinity of the (0|-1) level to the room temperature Fermi level and the lattice distortion, this may present as a detrimental charge trap in devices using selenium doped ZnTe.

Above a certain amount of selenium, a threshold manifests, above which these minority forms of selenium will begin altering the material's charge balance and normal defect chemistry. This threshold is near $10^{20}$ $cm^{-3}$ for the 800°C, 10 at% Zn tellurium melt discussed here. As with the distribution of selenium across its different forms, this point shifts with changes in the freeze-in temperature; higher growth temperatures will move it to slightly lower concentrations, and vice-versa. The main change to the native defect chemistry above this level is that the $Se_{Te}^{1}$ defect pushes the Fermi level farther away from the valence band at high temperatures, to maintain charge neutrality, which further increases the

zinc vacancy concentration and further decreases the tellurium vacancy concentration. This, in turn, decreases the room temperature hole concentration, as the Fermi level lies slightly deeper in the gap than before. In the language of canonical reaction schemes, the defect balance changes from $[v_{Zn}^{-1}] \approx [p]$ to $[v_{Zn}^{-1}] \approx [Se_{Te}^{+1}] + [p]$. Additionally, the $Se_{int}$-divacancy complex concentration exceeds $10^{14}$ $cm^{-3}$ near this threshold and continues increasing above it. This is expected to manifest as changes in ionized-impurity and lattice-deformation scattering rates at cryogenic temperatures, and the in-gap level associated with the $Se_{int}$-divacancy complex may become problematic as a trap state with higher selenium doping levels.

**Conclusions**

By leveraging statistical mechanics, density functional theory, and thermochemical modeling together, the results of this study resolve several long-standing questions about ZnTe, and reveal moderate concentrations of an unexpected native defect complex. First, these results have shown that the difficulties encountered when trying to produce n-type ZnTe directly from near-equilibrium techniques are caused by the unique combination of the systems equilibrium chemical potential space at temperature and the behavior of its native vacancies. This suggests that further efforts towards non-equilibrium donor doping techniques such as ion implantation may be more fruitful.

Second, it has been shown that the tellurium vacancy is the second most prevalent defect type in equilibrium ZnTe, with tellurium antisites and zinc interstitial defects occupying other, lower concentrations in the list of the systems top five highest concentration defect types; this helps resolve longstanding questions regarding what else is present in native ZnTe besides the zinc vacancy, and in what amounts. These results have additionally shown that there is a moderate concentration of $v_{Zn}$-$v_{Te}$ complex present in ZnTe. While this is not especially surprising given the propensity for chalcogenides to exhibit first nearest neighbor complexes between native defects and impurities, it is nevertheless noteworthy.

Third, we have shown that, in addition to incorporating purely as an alloying constituent on the Te sublattice, selenium unexpectedly behaves as a charged impurity, albeit at much lower levels than its overall concentration. At room temperature, 1/1000$^{th}$-1/10000$^{th}$ of the selenium behaves as a sub-valence-band localized hole trap, which only activates when the Fermi level is near the valence band, and which will eventually become part of the valence band as selenium exceeds the dilute limit. Even lower amounts of selenium form a first nearest neighbor complex with native vacancies, the $Se_{int}$-divacancy, which exhibits a transition level near the expected room temperature Fermi level, along with a moderate lattice distortion, and which may therefore become a problematic trap state at higher selenium concentrations. Together, these alternate forms of selenium perturb the underlying defect chemistry above about $10^{20}$ $cm^{-3}$, slightly increasing the zinc vacancy concentration and slightly decreasing the free hole concentration.

**Acknowledgements**

This work was supported by the U.S. Department of Energy Laboratory Directed Research and Development (LDRD) program within the Savannah River National Laboratory (SRNL). This work was produced by Battelle Savannah River Alliance, LLC under Contract No. 89303321CEM000080 with the U.S. Department of Energy. The publisher acknowledges the U.S. Government license to provide public access under the DOE Public Access Plan (http://energy.gov/downloads/doe-public-access-plan).

**TOC Graphic:**

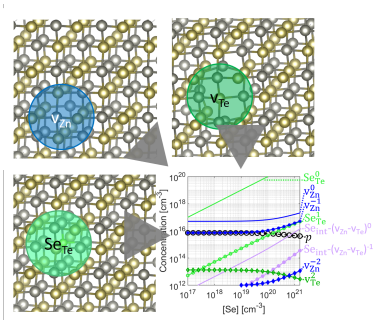


**References**


1. Mikhailik, V. B.; Galkin, S.; Kraus, H.; Mokina, V.; Hrytsak, A.; Kapustianyk, V.; Panasiuk, M.; Rudko, M.; Rudyk, V., ZnTe cryogenic scintillator. *Journal of Luminescence* **2017,** *188*, 600-603.
2. Tanaka, T.; Kume, Y.; Nishio, M.; Guo, Q.; Ogawa, H.; Yoshida, A., Fabrication of ZnTe Light-Emitting Diodes Using Bridgman-Grown Substrates. *Japanese Journal of Applied Physics* **2003,** *42* (Part 2, No. 4A), L362-L364.
3. Wu, Q.; Litz, M.; Zhang, X. C., Broadband detection capability of ZnTe electro-optic field detectors. *Applied Physics Letters* **1996,** *68* (21), 2924-2926.
4. Flender, R.; Sarosi, K.; Petracs, E.; Borzsonyi, A.; Chikan, V., Control of THz field waveform emitted from air plasma by chirping two-color laser pulses. *Optics Communications* **2019,** *436*, 222-226.
5. Gul, R.; Roy, U. N.; James, R. B., An analysis of point defects induced by In, Al, Ni, and Sn dopants in Bridgman-grown CdZnTe detectors and their influence on trapping of charge carriers. *Journal of Applied Physics* **2017,** *121* (11), 115701.
6. Roy, U. N.; Camarda, G.; Cui, Y.; Gul, R.; Hossain, A.; Yang, G.; Zazvorka, J.; Dedic, V.; Franc, J.; James, R., Role of selenium addition to CdZnTe matrix for room-temperature radiation detector applications. *Scientific reports* **2019,** *9* (1), 1-7.
7. Roy, U. N.; Camarda, G. S.; Cui, Y.; James, R. B., High-resolution virtual Frisch grid gamma-ray detectors based on as-grown CdZnTeSe with reduced defects. *Applied Physics Letters* **2019,** *114* (23).
8. Roy, U. N.; Camarda, G. S.; Cui, Y.; James, R. B., Characterization of large-volume Frisch grid detector fabricated from as-grown CdZnTeSe. *Applied Physics Letters* **2019,** *115* (24).
9. Aven, M., Mobility of Holes and Interaction between Acceptor Defects in ZnTe. *Journal of Applied Physics* **1967,** *38* (11), 4421-4430.
10. Flores, M. A., Defect properties of Sn- and Ge-doped ZnTe: suitability for intermediate-band solar cells. *Semiconductor Science and Technology* **2018,** *33* (1), 015004.
11. Dow, J. D.; Hong, R. D.; Klemm, S.; Ren, S. Y.; Tsai, M.; Sankey, O. F.; Kasowski, R. V., Proposed explanation of the p-type doping proclivity of ZnTe. *Phys Rev B Condens Matter* **1991,** *43* (5), 4396-4407.
12. Makhniy, V. P.; Protopopov, E. V.; Skripnik, N. V., Mechanism of tin diffusion in ZnTe single crystals. *Inorganic Materials* **2011,** *47* (9), 945-946.
13. Smith, F. T. J., A High Temperature Study of Native Defects in ZnTe. *Journal of Physics and Chemistry of Solids* **1971,** *32*, 2201-2209.
14. Varley, J. B.; Samanta, A.; Lordi, V., Descriptor-based approach for the prediction of cation vacancy formation energies and transition levels. *The Journal of Physical Chemistry Letters* **2017,** *8* (20), 5059-5063.
15. Larsen, T. L.; Stevenson, D. A., Electrical transport and defect levels in ZnTe crystals. *Journal of Applied Physics* **1973,** *44* (2), 843-847.

16. Yoshino, K.; Yoneta, M.; Yabe, T.; Ohmori, K.; Saito, H.; Ohisihi, M., Optical and electrical characterization of high-quality P-doped ZnTe substrates. *Physica B: Condensed Matter* **2003,** *340*, 254-257.
17. Tao, I. W.; Jurkovic, M.; Wang, W. I., Doping of ZnTe by molecular beam epitaxy. *Applied Physics Letters* **1994,** *64* (14), 1848-1849.
18. Title, R. M., G; Morehead, F., Self-Compensation-Limited Conductivity in Binary Semiconductors. II. n-ZnTe. *Physical Review* **1964,** *136* (1A), A300.
19. Sato, K. H., M.; Noda, A.; Arakawa, A.; Uchida, M.; Asahi, T;Oda, O., ZnTe pure green light-emitting diodes fabricated by thermal di!usion. *Journal of Crystal Growth* **2000,** *214*, 1080-1084.
20. Roy, U. N.; Bolotnikov, A. E.; Camarda, G. S.; Cui, Y.; Hossain, A.; Lee, K.; Lee, W.; Tappero, R.; Yang, G.; Gul, R.; James, R. B., High compositional homogeneity of CdTexSe1−x crystals grown by the Bridgman method. *APL Materials* **2015,** *3* (2), 026102.
21. Ait Raiss, A.; Sbai, Y.; Bahmad, L.; Benyoussef, A., Magnetic and magneto-optical properties of doped and co-doped CdTe with (Mn, Fe): Ab-initio study. *Journal of Magnetism and Magnetic Materials* **2015,** *385*, 295-301.
22. Goumrhar, F.; Bahmad, L.; Mounkachi, O.; Benyoussef, A., Calculated magnetic properties of co-doped CdTe(V, P): First-principles calculations. *Computational Condensed Matter* **2017,** *13*, 87-90.
23. Goumrhar, F.; Bahmad, L.; Mounkachi, O.; Benyoussef, A., Ab-initio calculations for the electronic and magnetic properties of Cr doped ZnTe. *Computational Condensed Matter* **2018,** *15*, 15-20.
24. Talwar, D. N.; Becla, P.; Lin, H.-H.; Chuan Feng, Z., Assessment of intrinsic and doped defects in Bridgman grown Cd1-xZnxTe alloys. *Materials Science and Engineering: B* **2021,** *269*.
25. Talwar, D. N.; Becla, P.; Lin, H.-H.; Feng, Z. C., Optical and structural characteristics of Bridgman grown cubic Zn1-xMnxTe alloys. *Materials Chemistry and Physics* **2018,** *220*, 460-468.
26. Imamura, M.; Tashima, D.; Kitagawa, J.; Asada, H., Magneto-optical properties of wider gap semiconductors ZnMnTe and ZnMnSe films prepared by MBE. *Journal of Electronic Science and Technology* **2020,** *18* (3).
27. Egarievwe, S. U.; Yang, G.; Egarievwe, A. A.; Okwechime, I. O.; Gray, J.; Hales, Z. M.; Hossain, A.; Camarda, G. S.; Bolotnikov, A. E.; James, R. B., Post-growth annealing of Bridgman-grown CdZnTe and CdMnTe crystals for room-temperature nuclear radiation detectors. *Nuclear Instruments and Methods in Physics Research Section A: Accelerators, Spectrometers, Detectors and Associated Equipment* **2015,** *784*, 51-55.
28. Egarievwe, S. U.; Chan, W.; Kim, K. H.; Roy, U. N.; Sams, V.; Hossain, A.; Kassu, A.; James, R. B., Carbon Coating and Defects in CdZnTe and CdMnTe Nuclear Detectors. *IEEE Transactions on Nuclear Science* **2016,** *63* (1), 236-245.
29. Kresse, G.; Furthmüller, J., Efficiency of ab-initio total energy calculations for metals and semiconductors using a plane-wave basis set. *Computational materials science* **1996,** *6* (1), 15-50.
30. Kresse, G.; Furthmüller, J., Efficient iterative schemes for ab initio total-energy calculations using a plane-wave basis set. *Physical review B* **1996,** *54* (16), 11169.
31. Kresse, G.; Joubert, D., From ultrasoft pseudopotentials to the projector augmented-wave method. *Physical review b* **1999,** *59* (3), 1758.
32. Heyd, J.; Scuseria, G. E.; Ernzerhof, M., Hybrid functionals based on a screened Coulomb potential. *The Journal of Chemical Physics* **2003,** *118* (18), 8207-8215.
33. Heyd, J.; Scuseria, G. E.; Ernzerhof, M., Erratum: “Hybrid functionals based on a screened Coulomb potential” [J. Chem. Phys. 118, 8207 (2003)]. *The Journal of Chemical Physics* **2006,** *124* (21), 219906.
34. Isik, M.; Gullu, H.; Parlak, M.; Gasanly, N., Synthesis and temperature-tuned band gap characteristics of magnetron sputtered ZnTe thin films. *Physica B: Condensed Matter* **2020,** *582*, 411968.

35. Togo, A.; Tanaka, I., First principles phonon calculations in materials science. *Scripta Materialia* **2015,** *108*, 1-5.
36. Baker, J. N.; Bowes, P. C.; Harris, J. S.; Irving, D. L., An informatics software stack for point defect-derived opto-electronic properties: the Asphalt Project. *MRS Communications* **2019,** *9* (3), 839-845.
37. Baker, J. N.; Bowes, P. C.; Irving, D. L., Hydrogen solubility in donor-doped SrTiO3 from first principles. *Applied Physics Letters* **2018,** *113* (13), 132904.
38. Barin, I.; Platzki, G., *Thermochemical data of pure substances*. 3rd ed.; Wiley Online Library: 1989.
39. M.W. Chase, J., C.A. Davies, J.R. Downey, Jr.; D.J. Frurip, R. A. M., A.N. Syverud, *NIST Standard Reference Database 13*. NIST: 1998.
40. Roy, U. N.; Burger, A.; James, R. B., Growth of CdZnTe crystals by the traveling heater method. *Journal of Crystal Growth* **2013,** *379*, 57-62.
41. Jacques Steininger, A. J. S., and Robert F. Brebrick, Phase Diagram of the Zn-Cd-Te Ternary System. *Journal of the Electrochemical Society* **1970,** *117* (10), 1305-1309.
42. Kroger, F. A., The P-T-x Phase Diagram of the System Zinc-Tellurium. *J. Phys. Chem.* **1965,** *69* (10), 3367-3369.
43. Harris, J. S. Point Defects in AlN and Al-Rich AlGaN from First Principles. PhD Thesis, North Carolina State University, 2019.
44. Kumagai, Y.; Oba, F., Electrostatics-based finite-size corrections for first-principles point defect calculations. *Physical Review B* **2014,** *89* (19), 195205.
45. *CRC Handbook of Chemistry and Physics*. 102 ed.; CRC Press: 2021.
46. Van de Walle, C. G.; Neugebauer, J., First-principles calculations for defects and impurities: Applications to III-nitrides. *Journal of Applied Physics* **2004,** *95* (8), 3851-3879.
47. Baker, J. N.; Bowes, P. C.; Long, D. M.; Moballegh, A.; Harris, J. S.; Dickey, E. C.; Irving, D. L., Defect mechanisms of coloration in Fe-doped SrTiO3 from first principles. *Applied Physics Letters* **2017,** *110* (12), 122903.
48. Kamata, A.; Yoshida, H.; Chichibu, S.; Nakanishi, H., Growth and doping characteristics of ZnSeTe epilayers by MOCVD. *Journal of crystal growth* **1997,** *170* (1-4), 518-522.